CHEMISTRY

Battery metal recycling by flash Joule heating

Weiyin Chen[1]†, Jinhang Chen[1]†, Ksenia V. Bets[2], Rodrigo V. Salvatierra[1], Kevin M. Wyss[1], Guanhui Gao[2], Chi Hun Choi[2], Bing Deng[1], Xin Wang[3], John Tianci Li[1], Carter Kittrell[1,4], Nghi La[1], Lucas Eddy[1,5], Phelecia Scotland[2], Yi Cheng[1], Shichen Xu[1], Bowen Li[1], Mason B. Tomson[3], Yimo Han[2], Boris I. Yakobson[1,2,4]*, James M. Tour[1,2,4,5,6]*

The staggering accumulation of end-of-life lithium-ion batteries (LIBs) and the growing scarcity of battery metal sources have triggered an urgent call for an effective recycling strategy. However, it is challenging to reclaim these metals with both high efficiency and low environmental footprint. We use here a pulsed dc flash Joule heating (FJH) strategy that heats the black mass, the combined anode and cathode, to >2100 kelvin within seconds, leading to ~1000-fold increase in subsequent leaching kinetics. There are high recovery yields of all the battery metals, regardless of their chemistries, using even diluted acids like 0.01 M HCl, thereby lessening the secondary waste stream. The ultrafast high temperature achieves thermal decomposition of the passivated solid electrolyte interphase and valence state reduction of the hard-to-dissolve metal compounds while mitigating diffusional loss of volatile metals. Life cycle analysis versus present recycling methods shows that FJH significantly reduces the environmental footprint of spent LIB processing while turning it into an economically attractive process.

INTRODUCTION

Battery metals are essential to produce cathode materials deployed in commercial secondary lithium-ion batteries (LIBs), especially for lithium, cobalt, nickel, and manganese (1, 2). Current strategies to collect battery metals from their natural reserves are resource and pollution intensive and unsustainable in the long term (3–6). For example, excessive acid leaching of the cobalt ore, followed by biphasic solvent extraction, chemical precipitation, and electrowinning, has been the typical processing route for leaching weathered cobalt ore (3) due to the associated mineral impurities and intrinsically low concentrations of cobalt (7–9). At the projected pace of nickel and cobalt mining, the world's reserves of these elements are predicted to be depleted by 2050 and 2030, respectively (4, 5, 8). The ever-increasing demand and the foreseeable shortage of reserves have encouraged the reclaiming of battery metals from other resources such as spent LIBs. It is predicted that the global market of the battery metals in spent LIBs will reach ~$22.8 billion in 2030 with a compound annual growth rate of ~20% (10). The battery metals account for ~30 weight % (wt %) of the battery (11), which is far higher than those in natural resources, especially for cobalt, nickel, manganese, and lithium [<1000 parts per million (ppm)] (8, 9). Therefore, spent LIBs are a local and promising alternative resource for the supply of battery metals. A closed-loop raw material solution for spent LIBs will lessen the need for mining of battery metals, diminish the environmental consequences of LIB disposal, and provide an economic incentive to recycle.

There have been several recycling strategies to collect the valuable metals contained in spent LIBs, including pyrometallurgy (12–14), hydrometallurgy (15–17), biometallurgy (18), and electrochemical extraction (19). Pyrometallurgy involves direct high-temperature smelting to reduce the transition metal oxidation states (12). Although ~100% recovery of transition metals can be achieved, extra activation steps are required to recover lithium from the slag (20). In addition, the pyrometallurgical method requires a high-temperature furnace that is highly energy consuming (19). The hydrometallurgical method also affords high yields by optimizing the leaching processes, including acid concentrations, additives, leaching temperature, and time (2). To achieve a high recovery yield of >95%, a large volume of concentrated inorganic acid and lengthy leaching steps are necessary, which produces problematic secondary wastes. The biometallurgical method involves the incubation of microbes and their metabolites to bioleach the metals, which can be economically and environmentally friendly (18). However, the long treatment period of several days to weeks can hinder its application on a large scale. Electrochemical extraction enriches the lithium from pretreated cathode materials with a lithium-selective membrane (19). However, a rapid and effective recycling method is desired that can achieve high extractability for all battery metals while maintaining a low environmental footprint.

Recent work has shown that electrical heating that is ultrafast, controllable, and energy efficient can be used for materials synthesis and processing (21–25). The carbothermal shock (21, 22) and flash Joule heating (FJH) (23–25) processes have been used to synthesize various nanomaterials with interesting structures and compositions, such as high-entropy alloys (21) and turbostratic graphene (23, 26). Programmable heating and quenching further demonstrates the high selectivity, stability, and efficiency of ultrafast high-temperature reactions for C_2 products and NH_3 synthesis (27).

Here, we show that the FJH process is used to activate diverse combinations of black mass, as it is known and routinely used in the industry, and contains a mixture of cathode and anode. A rapid electrothermal process can raise the temperature to >2100 K

[1]Department of Chemistry, Rice University, 6100 Main Street, Houston, TX 77005, USA. [2]Department of Materials Science and NanoEngineering, Rice University, 6100 Main Street, Houston, TX 77005, USA. [3]Department of Civil and Environmental Engineering, Rice University, 6100 Main Street, Houston, TX 77005, USA. [4]Smalley-Curl Institute, Rice University, 6100 Main Street, Houston, TX 77005, USA. [5]Applied Physics Program, Rice University, 6100 Main Street, Houston, TX 77005, USA. [6]NanoCarbon Center and the Welch Institute for Advanced Materials, Rice University, 6100 Main Street, Houston, TX 77005, USA.
*Corresponding author. Email: biy@rice.edu (B.I.Y); tour@rice.edu (J.M.T.)
†These authors contributed equally to this work.

with both fast heating and cooling rates of $>10^4$ K s^{-1}, leading to the thermal decomposition of the hard-to-dissolve compact solid electrolyte interphase (SEI) and other impurities. FJH also achieves carbothermal reduction of the transition metal compounds to their lower oxidation state or metal(0) counterparts, making them far easier to extract by dissolution. The FJH activation process of black mass boosts the leaching kinetics by ~1000-fold and enables an increase of recovery yields for battery metals to 286%, compared to the direct leaching by 1.0 M HCl. Simultaneously, the rapid electrothermal process alleviates the diffusional loss of volatile metals, such as lithium, compared with the continuous smelting process in the pyrometallurgical method (*12*). Therefore, all battery metals can be recovered together from the FJH-activated black mass with a high leaching efficiency of ~98%. In addition, FJH activation shows the adaptability for black mass with distinct cathode compositions, structures, and states of health (table S1). The FJH activation strategy is scalable and energy efficient with a low electrical energy consumption of ~234 kWh ton^{-1} or \$9.4 ton^{-1}. Life cycle analysis (*28*) comparisons to pyrometallurgy and hydrometallurgy methods indicate that the FJH activation can significantly reduce the total energy, water, acid consumption, and greenhouse gas (GHG) emissions, underscoring the favorable environmental and economic impact when applying FJH activation for spent battery recycling.

RESULTS

Acid-extractable battery metals in black mass

Seven types of black mass, named from BM-1 to BM-7, are used in this study (Table 1). The total content of battery metals from black mass, including lithium, cobalt, nickel, manganese, and iron, was quantified by the aqua regia analytical method (*29*). For BM-1, the total amounts of lithium and transition metals are 36.1 and 409.5 g kg^{-1}, respectively (fig. S1), which are much higher than the metal content from natural resources, underscoring that black mass is a preferred source for the supply of battery metals. Acid-leachable battery metals are extracted by 1.0 M HCl. Similar pH-dependent leachabilities are observed for all the black mass types. BM-1 shows the lowest recovery yield (Y_0) of ~34.2% (Fig. 1A); therefore, unless otherwise specified, BM-1 is the test case upon which we apply FJH as described below. By changing the acid concentration from 0.01 to 12.0 M, strong correlations between pH and Y_0 are observed for both lithium and transition metals (Fig. 1B). There is a rapid incline in Y_0 as the acid concentration increases, and only when the concentration is ≥6.0 M do the Y_0 values of lithium and transition metals exceed 90% (Fig. 1B).

The low Y_0 is attributed to limited thermodynamics and sluggish kinetics of dissolution. The black mass includes graphite and $Li_{0.68}CoO_2$, as shown in the x-ray diffraction (XRD) analysis (fig. S2). Compared to lithium cobalt oxide ($LiCoO_2$), partial delithiation causes the increase in the oxidation states (*30*) for cobalt in the bulk particles, although the surface reconstruction can trigger the partial reduction of oxidation states for cobalt from +3 to +2, as confirmed by high-resolution x-ray photoelectron spectroscopy (XPS) (Fig. 1C). However, there is a positive correlation between the oxidation state of metal and the Gibbs free energy change (ΔG) of the acid leaching reaction (Fig. 1D and table S2). Consequently, it becomes less thermodynamically favorable for the metallic compounds to dissolve in the acid solution as their oxidation state increases (*31*). For example (*2*), the solubility of Co^{3+} is $>10^8$ lower

Table 1. The categories of black mass used in our work. LT, low temperature; HT, high temperature.

Name	Materials and sources
BM-1	Raw black mass collected from spent commercial lithium batteries (LG Chem 112711, B052R785-9005A).
	Accurate cathode chemistry was not given (mainly $LiCoO_2$).
	Cell history: The battery composition is $LiCoO_2$. It has been charged and discharged for over 600 cycles. More specifically, 90% of the time the computer was plugged in; 5% of the time, the computer was used below 50% charge; and 5% time of the time, the computer was used below 10% charge. The battery was replaced when it did not hold charge well (<70% capacity retention) after 2 years usage.
BM-2	Simulated black mass prepared from $LiNi_{0.8}Mn_{0.1}Co_{0.1}O_2$ cathode (NMC811).
	Mass ratio between $LiNi_{0.8}Mn_{0.1}Co_{0.1}O_2$ and conductive carbon is ~2:1.
BM-3	Simulated black mass prepared from $LiNi_{0.8}Co_{0.15}Al_{0.05}O_2$ cathode (NCA) and graphite anode.
	Mass ratio between $LiNi_{0.8}Co_{0.15}Al_{0.05}O_2$ and graphite is ~2:1.
BM-4	Simulated black mass prepared from $LiFePO_4$ cathode (LFP) and graphite anode.
	Mass ratio between $LiFePO_4$ and graphite is ~2:1.
BM-5	Simulated black mass prepared from HT-$LiCoO_2$ cathode (HT-LCO) and graphite anode.
	Mass ratio between HT-$LiCoO_2$ and graphite is ~2:1.
BM-6	Simulated black mass prepared from LT-$LiCoO_2$ cathode (LT-LCO) and graphite anode.
	Mass ratio between LT-$LiCoO_2$ and graphite is ~2:1.
BM-7	Simulated black mass prepared from multiple cathodes ($LiNi_{0.8}Mn_{0.1}Co_{0.1}O_2$, HT-$LiCoO_2$, and $LiFePO_4$ cathode).
	Mass ratio between the multiple cathodes and graphite is ~2:1.
	Mass ratio of the cathodes—$LiNi_{0.8}Mn_{0.1}Co_{0.1}O_2$, HT-$LiCoO_2$, and $LiFePO_4$—is 1:1:1.

than that of Co^{2+} at the same pH. To compare the leachability, we used here 1.0 M HCl leaching as the standard protocol.

The repeated electrochemical cycling in LIBs incurs the accumulation of a compact SEI layer (*32–34*). XPS analyses show that the layer includes various organic and inorganic salts that precipitate as surface films on the electrodes (Fig. 1E and fig. S3). Scanning electron microscopy (SEM) and corresponding elemental analyses confirm the presence of binder and conductive carbon as impurities to impede the contact with the solution (Fig. 1F and fig. S4). The SEI effectively passivates the surface and prevents direct contact between the active materials and electrolyte, leading to parasitic reactions (*32*). The SEM images and corresponding elemental mappings verify the existence of partially etched microparticles with porous structures, even when extending leaching times to 24 hours (fig. S5). The remaining crystalline materials include $Li_{0.28}CoO_2$, Co_3O_4, and graphite, as shown in the XRD analyses (fig. S6). The amorphous surface layer and intact cathode core structure of the black mass after acid leaching are observed from high-resolution transmission electron microscopy (HR-TEM) and corresponding fast Fourier transform patterns (fig. S7). Hence, the SEI
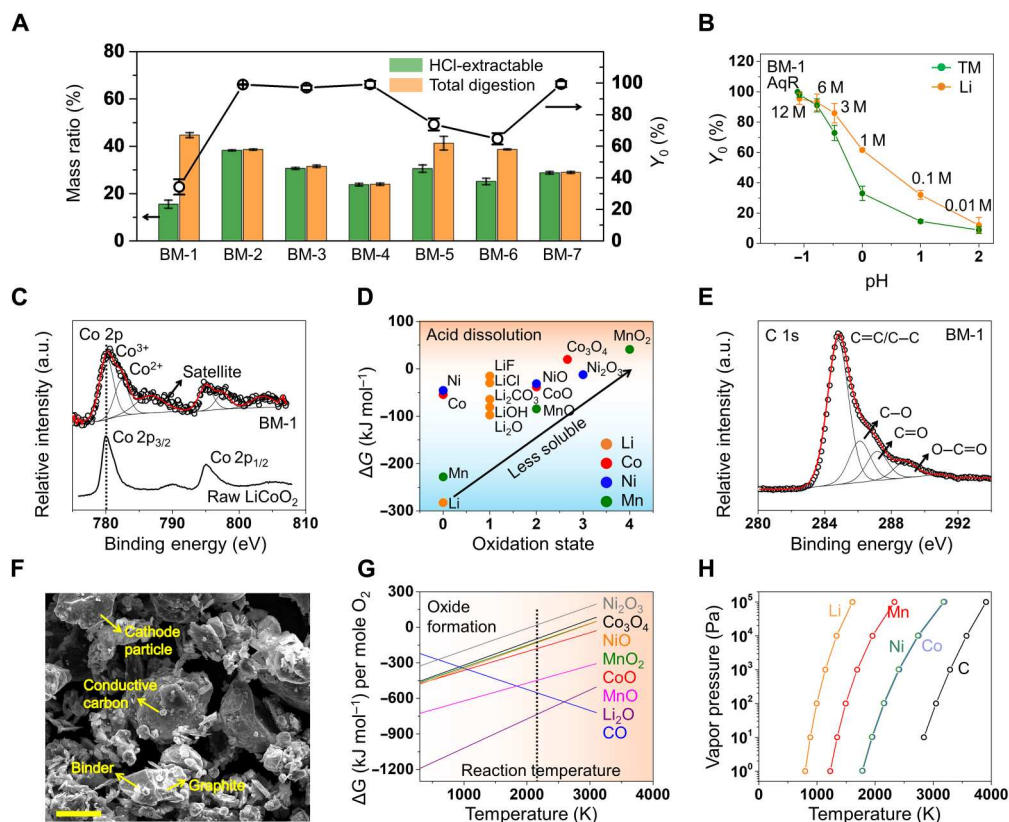
Fig. 1. Acid-extractable battery metals in black mass. (**A**) The HCl-extractable battery metal contents (1 M HCl, 50°C) and the total quantification of battery metals (aqua regia, 50°C) in various black mass types (BM-1 to BM-7; Table 1), and the recovery yield (Y_0) of the battery metals from black mass by 1 M HCl. The error bars reflect the standard deviations (SDs) from at least three individual measurements. The same below. (**B**) pH-dependent leachability of lithium and transition metals [HCl(aq), 50°C] from BM-1. (**C**) High-resolution Co 2p spectra of BM-1 and raw LiCoO$_2$. The dashed line shows the position of the Co peak in LiCoO$_2$ for comparison. a.u., arbitrary units. (**D**) Gibbs free energy of dissolution for metals and their corresponding metal compounds in 1 M HCl. (**E**) High-resolution C 1s spectrum of BM-1. (**F**) Scanning electron microscopy (SEM) image of BM-1. Scale bar, 10 μm. (**G**) Ellingham diagram of carbon monoxide and various metal oxides. The dashed line denotes the FJH temperature at ~2120 K. (**H**) Vapor pressure–temperature relationship of various battery metals and carbon. AqR, aqua regia; TM, transition metals.

passivation layer of the black mass affects the acid leaching rate, leading to slow dissolution kinetics and low leachability.

To solve the kinetic and thermodynamic restrictions of the acid leaching process, the removal of the SEI and the reduction of the battery metals are necessary. The 800-K calcination method can effectively remove the passivating SEI layer and other impurities due to their thermal instability (2) and further extended by the 2000-K reduction of the transition metal oxides (12, 35). Carbonaceous components such as graphite and conductive carbon can lower the reduction temperature to ~1800 K, as shown in the Ellingham diagram (Fig. 1G and table S3) (36). However, at this temperature, some battery metals have high vapor pressures, including lithium and manganese (Fig. 1H), leading to diffusional loss during the prolonged calcination process. Therefore, a rapid and high-temperature treatment is proposed here to address this problem (Fig. 2A and note S1).

Improved recovery yield of battery metals from black mass by FJH activation

In the FJH activation process, the raw, nonthermally treated black mass is directly used as the reactant without further treatment. Safety notes (37, 38) are listed in note S2. After loading the

powdered sample inside a quartz tube between two graphite electrodes, the resistance of the sample is controlled by the compression on the electrodes (Fig. 2B and fig. S8). The capacitor banks are connected to provide electrothermal energy to the reactant. Compared to the graphite and conductive carbon in the mixture, the cathode particles and SEI layer are more resistive and experience a larger power dissipation as anticipated by Joule's law (39). These local hotspots allow effective Joule heating, and they trigger the thermal transformation to activate the black mass, leading to the improvement of leachability (Fig. 2, B and C). Detailed flash parameters are listed in Table 2. For a typical FJH activation process with discharging voltage of 80 V, duration of 0.11 s, and resistance of 1.5 ohms, the peak current reaches ~104 A (Fig. 2D). The real-time temperature is recorded using a high-temperature infrared thermometer, showing a maximum temperature > 2100 K during the FJH activation process. The heating and cooling rate are ultrafast, at ~5.3 × 10^4 K s^{-1} and ~1.1 × 10^4 K s^{-1}, respectively (Fig. 2E). Because the FJH duration is short at ~0.11 s and the specific energy density is high at ~840 J g^{-1}, the specific input power reaches 7.6 kW g^{-1}, driving the rapid and high-temperature activation process. The product is called FJH-activated black mass, which is relatively stable even directly stored under ambient conditions. The average mass among
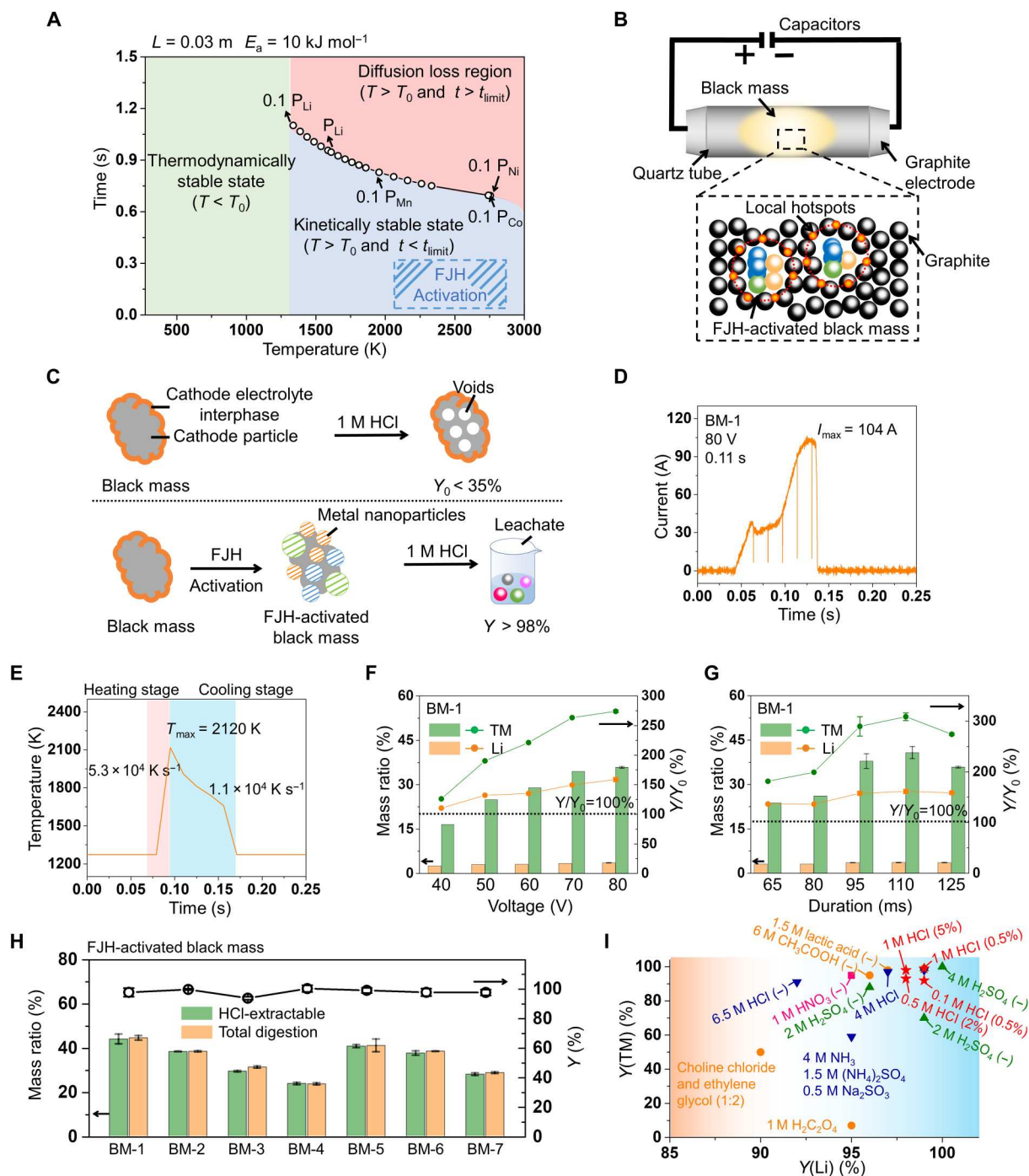
Fig. 2. Improved recovery yield of battery metals from different black mass by FJH activation. (A) The time- and temperature-dependent diagram underscoring the FJH activation process. **(B)** Schematic of the FJH activation of black mass, the local hotspots of resistive cathode particles, and **(C)** the acid leaching results with and without FJH activation. **(D)** Current-versus-time curve with the FJH activation condition of 80 V and 0.11 s. **(E)** Real-time temperature measurement with the FJH activation condition of 80 V and 0.11 s. Heating and cooling stages noted by color. **(F)** Relationship between the HCl-extractable battery metal contents (1 M, 50°C) from FJH-activated BM-1, increase in recovery yield (Y/Y_0), and the FJH voltages. The dashed line represents $Y/Y_0 = 100\%$, indicating the recovery result of BM-1. The error bars reflect the SDs from at least three individual measurements. The same below. **(G)** Relationship between the HCl-extractable battery metal contents (1 M, 50°C) from FJH-activated BM-1, increase in recovery yield (Y/Y_0), and the FJH durations. **(H)** The HCl-extractable battery metal contents (1 M, 50°C) from FJH-activated black mass and the total quantification of battery metals (aqua regia, 50°C) in various types of black mass, and the recovery yield (Y) of the battery metals from various FJH-activated black mass by 1 M HCl. **(I)** Comparison of recovery yields of lithium and transition metals by different leaching reagents, with concentration noted. The (−) indicates the usage of the reducing reagents. The red stars reflect the result from our work. Detailed parameters can be found in table S4.

Table 2. The optimized FJH activation conditions of different black mass materials. atm, atmosphere.

	FJH-activated BM-1	FJH-activated BM-1 (gram scale)	FJH-activated BM-2 (NMC811 cathode)
Reactant component	BM-1	BM-1	BM-2
Mass (mg)	200	2000	200
Reaction atmosphere	1-atm Ar	1-atm air	1-atm Ar
Reactant resistance (ohm)	1.5	0.6	1.5
Voltage (V)	80	120	80
Reaction time (ms)	110	VFD*	125
Capacitance (mF)	60	624	60
Flash repetitions	Two flashes	One flash	Two flashes
	FJH-activated BM-3 (NCA cathode)	**FJH-activated BM-4 (LFP cathode)**	**FJH-activated BM-5 (HT-LCO cathode)**
Reactant component	BM-3	BM-4	BM-5
Mass (mg)	200	200	200
Reaction atmosphere	1-atm Ar	1-atm Ar	1-atm Ar
Reactant resistance (ohm)	0.7	1.0	0.7
Voltage (V)	80	80	80
Reaction time (ms)	110	110	110
Capacitance (mF)	60	60	60
Flash repetitions	Two flashes	Three flashes	Two flashes
	FJH-activated BM-6 (LT-LCO cathode)		**FJH-activated BM-7 (Cathode mixtures)**
Reactant component	BM-6		BM-7
Mass (mg)	200		200
Reaction atmosphere	1-atm Ar		1-atm Ar
Reactant resistance (ohm)	0.7		0.7
Voltage (V)	80		80
Reaction time (ms)	110		110
Capacitance (mF)	60		60
Flash repetitions	One flash		Two flashes

*VFD is a type of controller that drives an electric switch by varying the frequencies and durations of its power supply. Here, 10% duty cycle for 1 s followed by 20% duty cycle for 4 s was used.

three FJH-activated black mass samples increases ~2.3% after 2 weeks placed in air. The difference can be ascribed to the water absorption of Co_3O_4 and slight oxidation of Co to CoO in air, as indicated by thermogravimetric analysis (TGA), high-resolution XPS, and XRD results (figs. S9 to S11 and table S4). The good stability of FJH-activated black mass is a crucial factor to maintain the digestion performance without the utilization of an inert atmosphere, leading to favorable operating cost and lower environmental footprint. The detailed life cycle assessments (LCAs) will be discussed below. The recovery yields of battery metals from FJH-activated black mass (Y) are calculated and compared with those of the starting black mass (Y_0) (note S3) (31). To exclude any contamination from other parts of the FJH equipment, the battery metal contents from the quartz tube, copper wool, and graphite spacers are measured, and they show $>10^3$ lower concentration of the measured elements (fig. S12). The metal contributions from the other parts are, therefore, ignored in the calculations.

As the flash voltage increases from 40 to 80 V, the leachability of lithium and transition metals increases (Fig. 2F). Further increase of the flash voltage causes the loss of the metals and lowers Y from the FJH-activated black mass (fig. S13). Similar improvement can be observed when increasing the flash duration from 65 to 110 ms with flash voltage at 80 V (Fig. 2G). At ~80 V and 110 ms, the 1.0 M HCl-extractable contents of lithium and transition metals are 35.2 and 407.0 g kg^{-1}, respectively, corresponding to the Y of both lithium and transition metals of ~98%. This result indicates that there are notable increases of the recovery yield (Y/Y_0) of lithium and transition metals to ~161 and 309%, respectively, compared with Y_0 of the black mass, ~62 and ~33% for lithium and transition metals, respectively, using 1.0 M HCl (Fig. 2, G and H). The pH-dependent leaching results of FJH-activated black mass are investigated and compared to those of black mass (fig. S14). As the acid concentration declines by 100× to 0.01 M HCl (pH 2), Y values of lithium and transition metals are ~74 and ~70% for FJH-activated black mass, substantially higher than those of black mass under the same leaching condition where $Y_0 \sim 12$ and ~9% for lithium and transition metals, respectively. These Y values are even higher than $Y_0 \sim 62$ and ~33% for lithium and transition

metals, respectively, at much higher acid concentration of 1.0 M HCl (pH 0). Although extending the leaching time to 168 hours, Y_0 values of black mass of ~40 and ~24% for lithium and transition metals, respectively, at 0.01 M HCl (pH 2) are not comparable to Y values of FJH-activated black mass of ~89 and ~93% for lithium and transition metals, respectively, using 0.01 M HCl (fig. S14). In addition, the acid leaching results of the black mass show the variation of transition metal–to–lithium atomic ratio in the leachates from 1.33 to 0.60 as the pH increases, while the atomic ratios are relatively constant at ~1.32 for the FJH-activated black mass, thus making the latter preferable to prepare the resynthesized cathodes (fig. S14 and note S3) (40). The leaching results of FJH-activated black mass, denoted by stars in Fig. 2I, are compared with hydrometallurgical (1, 15, 16, 29, 41–51) and pyrometallurgical (12, 13, 36, 52–54) methods, highlighting the low acid concentrations required, high pulp density, and superior leaching efficiencies obtained for the FJH activation strategy (fig. S15 and table S5). In addition, the recovery yields of battery metals are not significantly affected by the electrolyte and salt residue (fig. S16). The leachable metal contents of washed black mass slightly decreased compared to the unwashed black mass possibly due to the removal of electrolyte, salt, and SEI layer. The results indicate that the electrode after treatment is not required in the FJH activation strategy.

Mechanism of the improved battery metal extractability by the FJH activation

The acid leaching kinetics of FJH-activated black mass is studied and compared to those of black mass. Y of FJH-activated black mass increases at faster rates than Y_0 of black mass. In addition, even after ~25 hours, Y_0 values of lithium and transition metals are only ~76 and ~44%, respectively, using 1.0 M HCl (Fig. 3A and fig. S17), while nearly complete dissolution of the battery metals is achieved for FJH-activated black mass. The relationship between the acid leaching rate and the reaction progress for both lithium and transition metals is discussed and plotted (Fig. 3, B and C, and note S4). On average, the acid leaching rates of lithium and transition metals for FJH-activated black mass are ~100- and ~1000-fold faster, respectively, than those of black mass. Because most transition metals are cobalt ions for BM-1 (fig. S1), the distribution of cobalt ion in the leachates is determined by ultraviolet-visible (UV-vis) absorbance spectra (fig. S18) (55), which demonstrates that the leaching efficiency improvements of transition metals are mainly attributed to the increase of Co^{2+} in the leachates (Fig. 3D and fig. S19), indicating effective carbothermal reduction of the transition metals.

The FJH activation also increases the surface area of the black mass from ~3.3 to ~7.1 $m^2 g^{-1}$, corresponding to an increase of ~115% (Fig. 3E). A similar ~250% increase in the concentration of nanopores is observed from the pore size distribution (fig. S20). The abundant surface area and nanopores allow direct contact between the black mass and the acid solution, promoting the high leaching efficiency liquid-solid reaction. The FJH-activated black mass includes metals(0), metal oxides, and salts (Fig. 3F), which are the decomposition products of the SEI and the cathode particles, as confirmed by the XRD analyses. The elemental analysis of cobalt also indicates that Co^{2+}/Co^{3+} ratio increased significantly and Co^{2+} is the dominant species for FJH-activated black mass even at the surface, validating the carbothermal reduction of cobalt

species with high oxidation states during the FJH activation process (fig. S11).

The gaseous products were further analyzed by gas chromatography–mass spectrometry (GC-MS) as shown in Fig. 3G and figs. S21 and S22. In total, ~20 different gaseous species were detected, including simple oxides, such as carbon monoxide and carbon dioxide; oxygenated organic compounds: ethers, aldehydes, and esters; nonfunctionalized hydrocarbons: alkenes, benzene, and toluene; as well as fluorinated hydrocarbons such as 1,3,5-trifluorobenzene and fluorinated butadiene. However, no HF or F_2 was observed in the gaseous products. Therefore, we propose that the organic component of the SEI is fully decomposed to C_2-C_5 molecules after the FJH activation. The inorganic components also partially decompose, and small molecules, such as Li_2O and LiF, form, as confirmed by XRD and XPS results (Fig. 3F and fig. S11). The decomposition of the SEI components can also be verified by TGA results (fig. S10), due to the near absence of weight loss at a rather low temperature (<550°C) for FJH-activated black mass.

First-principles calculations show the energy preference, ΔE, of the phase segregation between $LiCoO_2$ and $Co_3O_4 + O_2$ (fig. S23). Relatively low ΔE are observed in cathodes with nearly stochiometric composition compared to aged ones where a substantial degree of delithiation is observed. This result indicates the increased effectiveness of the thermal decomposition during the FJH activation of heavily degraded cathode particles (56, 57). The microscale and nanoscale morphologies of FJH-activated black mass are shown in Fig. 4 (A and B). These crystalline materials, with primary particle sizes ranging from 10 to 50 nm, are contacted with carbon materials (fig. S24), which facilitates electrochemical etching during the leaching, enhancing dissolution kinetics. The partially graphitized carbon crust allows permeability of metal ions, which is also crucial for the leaching process. The simulation at high annealing temperature of ~2500 K indicates an amorphous carbon structure with the density of 0.9 $g cm^{-3}$ (Fig. 4C). First-principles calculations show substantial effect of various structural elements within the amorphous carbon crust on the lithium-ion diffusion (figs. S25 and S26 and note S5) due to the increased lithium binding to undercoordinated carbon atoms (58). The annealing eliminates unpassivated graphitic edges and point defects, thus improving lithium-ion permeability of the crust (see sample trajectory, Fig. 4C) and acid leaching kinetics, as observed in the experiment. In addition, these nanoparticles stack together to form secondary particles with sizes up to 2 μm. These secondary particles further aggregate to form larger microparticles of ~30 μm as shown in Fig. 4D. The elemental mapping of the FJH-activated black mass confirms that the secondary particles (Fig. 4D) and the primary particles (Fig. 4E and fig. S27) consist of reduced transition metals due to the dispersive distribution of oxygen. The loosely formed hierarchical structure allows for the infiltration of acid during the leaching process, and it accelerates the liquid-solid reaction. After the same acid leaching process for FJH-activated black mass, there are only graphite microparticles with few if any metal micro- or nanoparticles (fig. S28). Only graphite patterns without the metal oxides or salts are detected as shown in the XRD spectrum (fig. S29), indicating the nearly complete collection of the battery metals from the powder mixture. In conclusion, the improvement of the leachability is attributed to transition metal reduction, passivation layer decomposition, and surface area increases together with a hierarchical structure change.
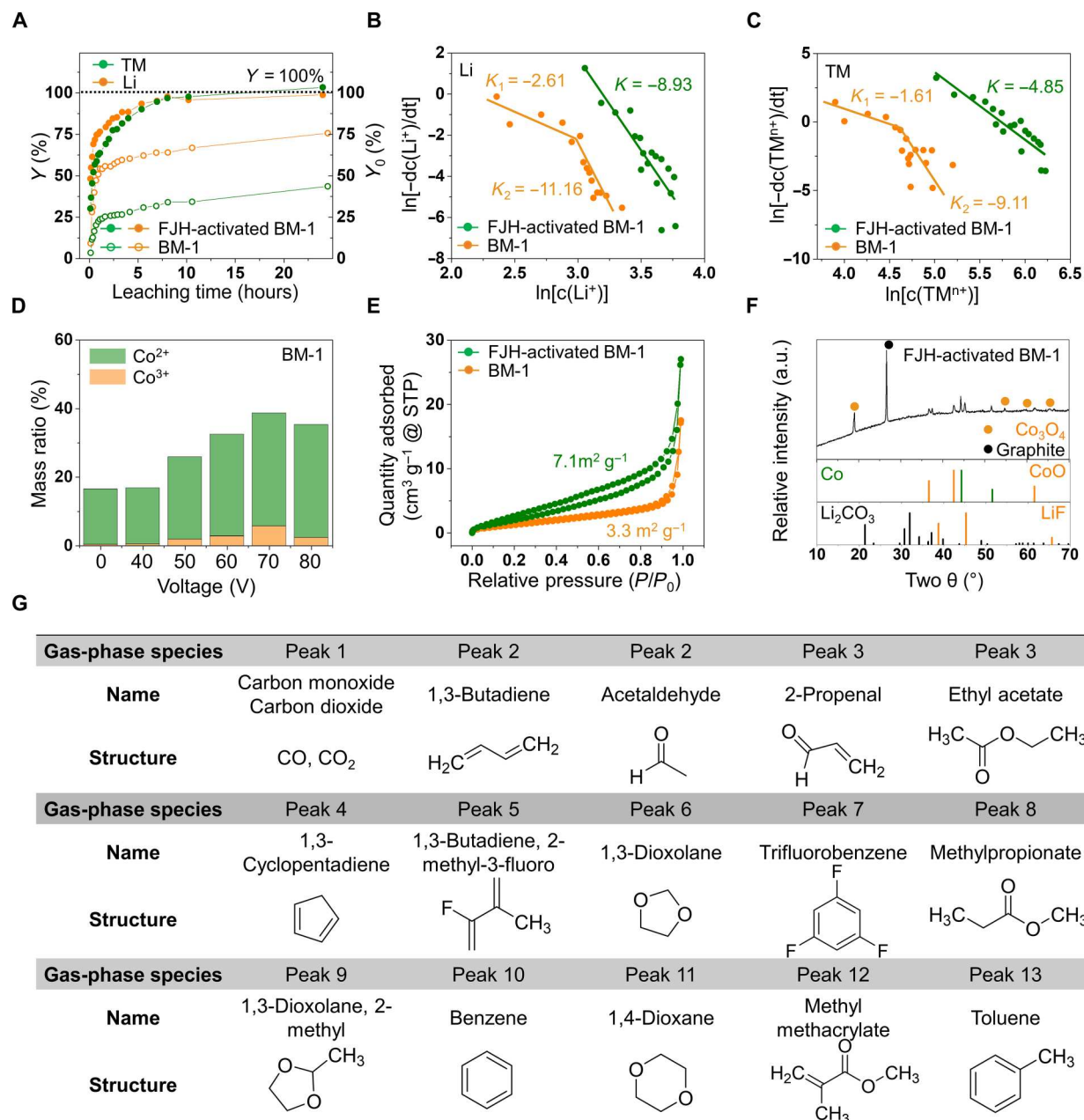
Fig. 3. Mechanism of the improved battery metal extractability by the FJH activation. (**A**) The kinetic leaching recovery yield of the BM-1 (Y_0) and FJH-activated BM-1 (Y) with 1 M HCl solution (50°C). (**B**) Relationship between kinetic lithium leaching rate and the concentration of Li^+ in the leachate. The slopes of fitting lines are given for different leaching stages. The same below. (**C**) Relationship between kinetic transition metal leaching rate and the concentration of total transition metal ions in the leachate. (**D**) Relationship between the concentration of Co^{2+}, Co^{3+} from the HCl-extractable battery metal contents of FJH-activated BM-1 (1 M HCl, 50°C), and the flash voltages. (**E**) Nitrogen adsorption and desorption curves at standard temperature and pressure (STP) reporting the surface areas of the raw and FJH-activated BM-1. (**F**) XRD pattern of FJH-activated BM-1. Powder diffraction file: 00-056-0159, graphite; 00-015-0806, Co; 04-005-4912, CoO; 04-020-7500, Co_3O_4; 04-007-3587, LiF; 04-010-5115, Li_2CO_3. (**G**) Gaseous products formed by the FJH activation.

Economic and environmental analysis of the FJH activation recycling process

The prospective cradle-to-gate LCA is considered using GREET 2020 and Everbatt 2020 (*59*, *60*), software developed by Argonne National Laboratory, which consists of the economic and environmental impacts from the collection of battery metals from spent LIBs (cradle) through all reaction processing involving the production of ~0.35 kg of cathode materials at the factory (gate). A cradle-to-gate life cycle analysis does not consider the use of the cathode materials nor their disposal (grave) because it is assumed that unused cathodes and recycled cathodes have the same usage and recycling stages. Three methods are analyzed and compared (note S6), including the hydrometallurgical (Fig. 5A), pyrometallurgical (Fig. 5B), and FJH activation recycling methods
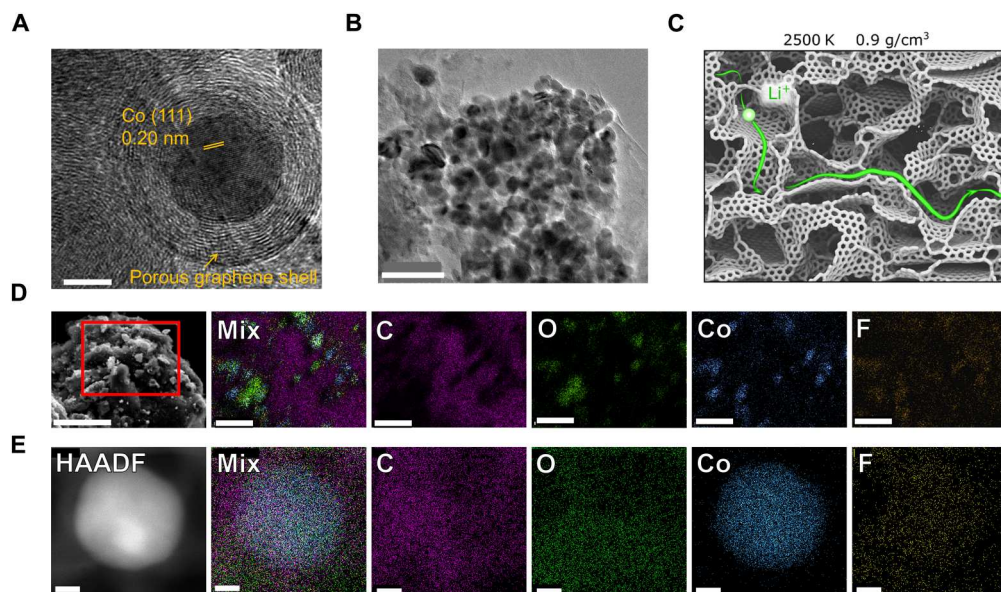
Fig. 4. Microscale characterization of FJH-activated black mass. (**A**) HR-TEM of the FJH-activated BM-1. Scale bar, 5 nm. (**B**) TEM images of the FJH-activated BM-1. Scale bar, 100 nm. (**C**) Li^+ permeating partially graphitized amorphous carbon structure at the end of 9-ns simulated annealing at 2500 K, where the green line indicates the calculated Li^+ trajectory. (**D**) Microscale morphology and corresponding element distributions about secondary particles of FJH-activated BM-1. Scale bars (elemental mapping results), 2 μm. (**E**) Nanoscale morphology and corresponding element distributions in primary particles of FJH-activated BM-1. Scale bars (elemental mapping results), 10 nm.

(Fig. 5C). A cutoff approach is used in these methods, and the environmental impacts of the spent batteries are associated with the prior product, and they are considered as battery waste without their related burdens (*28*).

The life cycle inventories with detailed parameters regarding the inputs and outputs of each individual step for the above methods are listed in table S6. Thus, the cradle-to-gate LCA (Fig. 5, D to H) reflects that the FJH activation recycling method decreases the consumption of concentrated HCl by ~87%, water consumption by ~26%, energy consumption by ~15%, and GHG emissions by ~23%, compared to the hydrometallurgical method. These values are attained by the optimization of the pretreatment, including the thermal treatment and its duration and the leaching processes (fig. S30). Therefore, the estimated cost in treating 1 kg of spent batteries to produce ~0.35 kg of cathode materials is calculated to be ~49% lower than the hydrometallurgical method. Larger improvements are observed when comparing the FJH activation recycling method with the pyrometallurgical method. The FJH activation recycling method reduces the usage of concentrated HCl by ~59%, water consumption by ~52%, energy consumption by ~26%, and GHG emissions by ~38%, reflecting the decrease in the environmental footprint and leading to the decrease in estimated cost by ~28% (Fig. 5, D to H) compared to the pyrometallurgical method.

DISCUSSION

Copper and aluminum are used as the anode and cathode current collectors in LIBs, respectively. These two metals are considered the major impurities during battery dismantlement and separation. In particular, for copper, when the concentration exceeds ~50 ppm, the electrochemical performance of the cathode active materials will be negatively affected. A recent report has also demonstrated that aluminum introduction can achieve the upcycling of cathode waste from $LiCoO_2$ to $LiNi_{0.8}Co_{0.15}Al_{0.05}O_2$ for a higher specific capacity and better cycling performance (*61*). The content of copper and aluminum in the FJH-activated samples are quite low (Al < 60 ppm and Cu < 30 ppm), suggesting a low impurity level (fig. S31 and table S7). The low concentration of copper is expected, because carbothermal reduction of the copper ion results in a more positive ΔG, thermodynamically preventing the dissolution by nonoxidative acids such as HCl (table S2). In addition, this carbothermal reduction temperature is ~700 K (table S3), indicating that copper ion is more easily reduced compared to other battery metals.

Because the postsyntheses of the cathode materials from the leachates are well studied in the hydrometallurgical method (*40*), the preparation of the resynthesized cathodes can be achieved using the leachates collected from FJH-activated black mass by following the same procedures, including coprecipitation and high-temperature sintering (*40*). The separation of the battery metals from the leachates is energy intensive and not necessarily required, because the battery compositions are shifting to the multicomponent transition metal oxides with layered or rocksalt-like structures for high energy densities (*62, 63*). As a demonstration, the $LiCoO_2$ cathode powder is resynthesized from the leachate of FJH-activated black mass (fig. S32) with a high reaction yield of >95%. The resynthesized cathode shows good crystallinity with a layered structure, as confirmed by XRD patterns (fig. S33). The electrochemical performance of the resynthesized $LiCoO_2$ cathode is then tested, exhibiting a high specific capacity of ~150 mAh g^{-1} in the initial cycles and good cycling stability (fig. S34).

The adaptability of the FJH activation recycling strategy is demonstrated here using seven different types of the black mass, from BM-1 to BM-7. Each shows distinct structures, chemistries, and state of health (Table 1 and note S7). Similar carbothermal
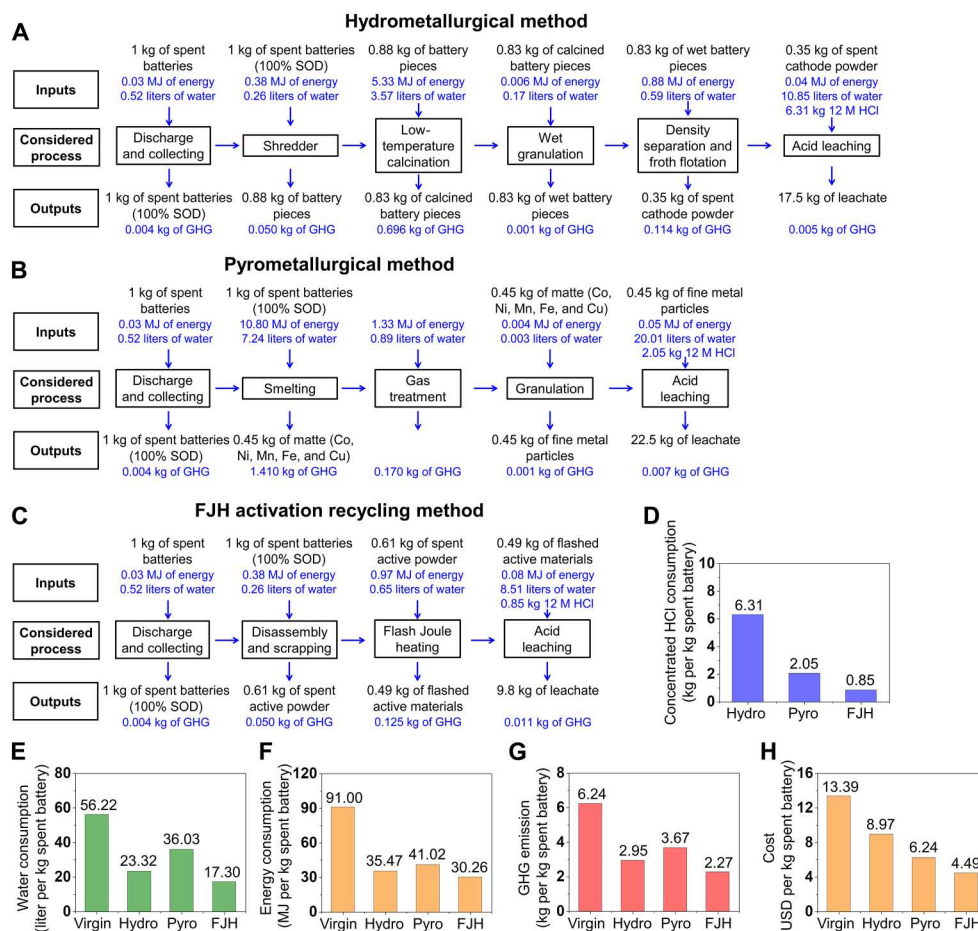
Fig. 5. Economic and environmental analysis of the FJH activation recycling process. (**A** to **C**) Process flow diagrams of various spent lithium-ion battery recycling routes, displaying the life cycle inventory including all considered inputs and outputs. Incidental inputs and outputs are shown in blue font to differentiate them from explicit inputs and outputs. (A) Hydrometallurgical method. (B) Pyrometallurgical method. (C) FJH activation recycling method. (**D**) Concentrated 12 M HCl consumption in treating 1 kg of spent batteries. (**E** to **H**) Water consumption, energy consumption, GHG emission, and cost analysis in treating 1 kg of spent batteries followed by producing ~0.35 kg of cathode materials from the leachate. The effects of producing the same amount of cathode materials from mining the virgin ores are given as a comparison and it is labeled as "Virgin." Hydro, hydrometallurgical method; Pyro, pyrometallurgical method; FJH, flash Joule heating activation recycling method.

reduction and formation of the simple oxides, salts, and metals are observed for BM-1 to BM-7 (figs. S35 to S40), leading to large improvements of the leaching efficiencies. The average Y/Y_0 values are ~138 and ~202% with 1.0 M HCl (Figs. 1A and 2H) and 0.1 M HCl (fig. S41), respectively. In the FJH-activation method, the effect of cell history on the recovery yield is likely not substantial. First, the high temperature during FJH-activation is enough to destroy the structure of the cathode materials and reduce the battery metals to simple metal oxides and metals. These results contribute to the enhanced leaching yield thermodynamically as demonstrated in Fig. 1. Second, for the cathode active materials, the cell history will mainly affect their surface structure, including the surface reduction due to oxygen atom loss, heterogeneous mixtures between lithium and other battery metals such as Li^+ and Ni^{2+}, as well as the surface structure evolution and passivation layer growth up to several hundred nanometers (*2*, *64*). However, we have established that FJH-activation achieves the thermal decomposition of the passivated SEI. The cathode materials with different structures (BM-5 and BM-6) and different cell histories (BM-1 and BM-5) do

not affect the leaching yield after the FJH-activation process. Therefore, FJH-activation method is less likely influenced by the cell history compared to hydrometallurgical and pyrometallurgical methods.

The potential scalability of the FJH activation strategy is discussed in note S8. To maintain the specific energy density, several general strategies are listed, including increasing the capacitance, flash repetitions, and voltages. Here, the gram-scale experiment can be carried out. The programmed heating and cooling strategy is applied by variable frequency drive (VFD) to better control the electrothermal reaction (Table 2). The real-time current with on/off status and the peak current of ~215 A are shown in fig. S42. Because the production rate of flash graphene (>10 kg day^{-1}) has been achieved in our laboratory via an automated system, the conceptual design of a continuous FJH reactor for black mass activation is further shown in fig. S43. Therefore, the FJH process can presumably be integrated into a continuous system for future production. In addition, the FJH method for making graphene is being industrially scaled up to 1 ton day^{-1} by mid-2023 and eventually targeted

for 100 tons day^{-1} per factory (*65*), and that requires even a higher temperature (>3000 K) and a larger energy density (~3.6 kJ g^{-1}) than the LIB recycling described here. The graphitic solid residue from the acid bath can be further used for recycled anodes as we demonstrated previously (*66*), thereby increasing the economic viability of this FJH approach.

MATERIALS AND METHODS
Materials
The LiCoO$_2$ (99.8% trace metal basis, 442704-100G-A) was purchased from MilliporeSigma. Cathode nickel-manganese-cobalt (LiNi$_{0.8}$Mn$_{0.1}$Co$_{0.1}$; EQ-Lib-LNCM811) powder was purchased from MTI Corporation. Lithium iron phosphate (LiFePO$_4$; battery grade, 0011512) was purchased from MTI Corporation. Lithium nickel–cobalt–aluminum oxide (LiNi$_{0.8}$Co$_{0.15}$Al$_{0.05}$; >98%, 760994-10G) was purchased from MilliporeSigma. Spent commercial lithium batteries (LG Chem 112711, B052R785-9005A) were obtained from 5-year-old Lenovo laptop computers. The cobalt(II) nitrate hexahydrate [Co(NO$_3$)$_2$ 6H$_2$O; > 98%, ACS reagent, 239267-5G] was purchased from MilliporeSigma. The cobalt(II) chloride (CoCl$_2$; 97%, 232696-5G) was purchased from MilliporeSigma. The ammonium thiocyanate (NH$_4$SCN; >97.5%, ACS reagent, 221988-100G) was purchased from MilliporeSigma. The lithium carbonate (Li$_2$CO$_3$; 99.99% trace metal basis, 431559-50G) was purchased from MilliporeSigma. The cobalt(II,III) oxide (Co$_3$O$_4$; 99.5% trace metal basis, 637025-25G) was purchased from MilliporeSigma. Carbon black [average particle size (APS), 10 nm; Black Pearls 2000] was purchased from Cabot Corporation. Quartz tubing [inside diameter (ID) = 8 mm, length (*L*) = 6 cm] was used for small batches (200 mg per batch), and quartz tubing (ID = 16 mm, *L* = 10 cm) was used for larger batches (2.0 g per batch) in the experiments. The standard solutions for inductively coupled plasma optical emission spectroscopy (ICP-OES) tests included cobalt standard (1000 ± 2 mg/liter, 30329-100ML-F), lithium standard (998 ± 4 mg/liter, 12292-100ML), manganese standard (1003 ± 5 mg/liter, 74128-100ML), nickel standard (998 ± 4 mg/liter, 28944-100ML-F), and iron standard (1001 ± 2 mg/liter, 43149-100ML-F), all of which were purchased from MilliporeSigma. The nitric acid (HNO$_3$; trace metal grade, 1120060) was purchased from Fisher Chemical, and hydrochloric acid (HCl; 99.999% trace metal basis, 339253-100ML) was purchased from MilliporeSigma. Water (HPLC Plus, 34877-4 L) was purchased from MilliporeSigma. Millipore Express polyethersulfone (PES) membrane filter unit (0.22 μm) was purchased from MilliporeSigma. In the work, seven different types of black mass were tested on the basis of their chemistries and structure as listed in Table 1. For the electrochemical test, *N*-methyl pyrrolidone (NMP; >99.0%, 443778-500ML) was purchased from MilliporeSigma. Polyvinylidene fluoride (PVDF) binder (121120-80G) was purchased from MTI Corporation. High conductive acetylene black (ABHC-01, 342431) was purchased from Soltex Corporation. The milling ball (Yttrium stabilized ZrO$_2$, 99.5%, radius (*R*) = 5 ± 0.3 mm) was purchased from MTI Corporation. The 1 M LiPF$_6$ in a mixture of ethylene carbonate (EC), diethyl carbonate (DEC), and dimethyl carbonate (DMC) (V:V:V = 1:1:1) electrolyte (battery grade, 901685-100ML) was purchased from MilliporeSigma. Lithium chip [diameter (*D*) = 16 mm, thickness (*t*) = 0.6 mm, 99.9% Li] was purchased from MTI Corporation.

FJH reaction
The FJH system was detailed in our previous publications (*23*). A circuit diagram of the FJH setup and the FJH reaction box used in the experiments were shown in fig. S8 with essential safety precautions (note S2) for the FJH system (*23*). The spent LIBs were discharged on a circuit until the voltage was below 2.5 V, and then the electrodes were collected by manually disassembling the spent batteries. The black mass is prepared by mixing the cathode and anode wastes directly collected from the spent electrodes. The raw black mass was mixed evenly by grinding with a mortar and pestle for ~10 min. The reactants were loaded into a quartz tube with an inner diameter of 8 mm. The mass loads in 8-mm tube were 200 mg. Graphite rods and copper wool were used as electrodes and spacers, respectively. They were used to compress the reactants as shown in Fig. 2B. The graphite rods were in contact with the sample in the quartz tube. The electrical energy was provided by a capacitor bank in the circuit with a total capacitance of 60 mF (8-mm tube). The capacitor bank was charged by a dc supply that could reach 400 V. The flash duration was controlled by an Arduino controller relay in the circuit acting as a high-speed switch. Various black mass materials, as listed in Table 1, were also used to demonstrate the versatility of the FJH activation method. After the FJH reaction, the reaction was permitted to cool for 3 min. For the scale-up trials, the VFD was used, which is a type of controller that drives an electric switch by varying the frequencies and durations of its power supply. The mass loads in 16-mm tube were 2.0 g. Here, 10% duty cycle for 1 s followed by 20% duty cycle for 4 s was used. The FJH voltage and capacitance were 120 V and 624 mF, respectively.

Low-temperature LiCoO$_2$ synthesis
The lithiated spinel low-temperature LiCoO$_2$ samples were synthesized by a solid-state reaction as shown in previous literature (*67*). Stoichiometric amount of Li$_2$CO$_3$ and Co$_3$O$_4$ was homogeneously mixed by grinding with a mortar and pestle for ~10 min. In the experiment, we used ~1.11 g of Li$_2$CO$_3$ and 2.41 g of Co$_3$O$_4$, respectively. Then, the powder mixture was heated at 400°C with a heating rate of 5°C min^{-1} under air. The temperature was kept at 400°C for 120 hours, followed by the slow furnace cooling. The commercial LiCoO$_2$ sample has a layered structure and belongs to the high-temperature LiCoO$_2$.

Characterization
The reactant and FJH products were characterized through SEM using a FEI Helios NanoLab 660 DualBeam SEM at 5 kV with a working distance of 4 mm. TEM images and selected area electron diffraction patterns were taken with a JEOL 2100F field emission gun TEM at 200 kV. Atomic resolution HR-TEM and high-angle annular dark-field scanning TEM (HAADF-STEM) images were taken with FEI Titan Themis S/TEM instrument at 80 keV after accurate spherical aberration correction. XPS data were collected with a PHI Quantera SXM scanning x-ray microprobe with a base pressure of 5×10^{-9} torr. Survey spectra were recorded using 0.5-eV step sizes with a pass energy of 140 eV. Elemental spectra were recorded using 0.1-eV step sizes with a pass energy of 26 eV. All the XPS spectra were corrected using the C 1s peaks (284.8 eV) as reference. For the depth analysis, an Ar$^+$ ion sputtering source was used to etch the surface layer. The average etching rate was calibrated and was ~7 nm min^{-1} in the experiment that can be further used to estimate the depth (*11*). XRD measurements were done by a Rigaku SmartLab

Intelligent XRD system with filtered Cu Kα radiation (λ = 1.5406 Å). The reactants and FJH products were analyzed on solid, dried samples using a Thermo Scientific Nicolet 6700 attenuated total reflectance Fourier-transform infrared spectrometer (Waltham, MA). TGA was performed on a Mettler Toledo TGA/DSC 3+ system. TGA data were collected at a heating rate of 20°C min^{-1} from 25° to 300°C and 10°C min^{-1} from 300° to 800°C under air. The air flow was set to 80 ml min^{-1}.

Sample digestion, leaching, and ICP-OES measurement

For all the black mass and FJH-activated black mass samples, the contents of acid-extractable battery metals, including lithium, cobalt, nickel, manganese, and iron, were measured. The aqueous HCl and total battery metal quantification were conducted. For total battery metal quantification, ~20 mg of black mass samples were digested in 3.0 ml of aqua regia at 50°C for 90 min. The aqua regia was prepared by mixing the nitric acid and hydrochloric acid in a molar ratio of ~1:3. The samples were filtered with PES membrane (0.22 μm) and diluted using HPLC plus grade water for ICP-OES measurement. For HCl leaching, ~20 mg of black mass samples were digested in ~5.0 ml of 1.0 M HCl solution at 50°C for 90 min. The samples were filtered with PES membrane (0.22 μm) and diluted using HPLC plus grade water for ICP-OES measurement. The standard procedure for leaching is with 1.0 M HCl solution at 50°C for 90 min as shown above if not mentioned specifically.

The pH-dependent leaching dynamics were investigated by using HCl solutions with various concentrations, including 0.01, 0.1, 1.0, 3.0, 6.0, and 12.0 M, respectively, as the leaching agents. The acid amounts were excess (~10× compared to the total metal amounts) to avoid obvious pH changes during the leaching tests. The leaching time and temperature were controlled the same as the total battery metal quantification tests for comparison.

For the kinetical leaching tests, ~100 mg of black mass samples were digested in 25.0 ml of 1.0 M HCl solution at 50°C. Solutions (~0.20 ml) were collected after the respective leaching time. They were filtered with PES membrane (0.22 μm) and diluted using HPLC plus grade water for the ICP-OES measurement.

The metal content in the samples was quantified using a PerkinElmer Optima 8300 ICP-OES system. The samples were diluted with a 2% aqueous solution of nitric acid, and calibration curves were generated using seven ICP standard solutions (blank solution, 1, 2, 5, 10, 25, and 50 ppm solutions), with the only results used from correlation coefficients that were greater than 0.999. The gas nebulizer flow rate range was set between 0.45 and 0.75 liters min^{-1}, and two wavelengths per element were used in the axial mode unless otherwise stated: cobalt (228.616 and 230.786 nm), lithium (670.784 nm—radial mode—and 610.362 nm), nickel (231.604 and 341.476 nm), manganese (257.610 and 259.372 nm), and iron (238.204 and 239.562 nm).

Determination of Co^{2+} and Co^{3+} via UV-vis measurement

Various concentrations of the Co(NO$_3$)$_2$ solutions were prepared (blank solution, 0.001, 0.002, 0.005, 0.010, 0.020 M) to generate the calibration curves. Stoichiometric amounts of 2 M NH$_4$SCN was added dropwise in the above standard solutions and solutions prepared from FJH-activated samples to enhance the sensitivity of the solutions. UV-vis (Shimadzu UV-3600 plus) was used to collect the spectra of these standard solutions. The calibration curve (fig.

S18) was used to calculate the concentration of Co^{2+} in the samples. The amount of Co^{3+} was calculated on the basis of Eq. 1

$$n(\text{Co}^{3+}) = n(\text{Co}^{\text{total}}) - n(\text{Co}^{2+}) \tag{1}$$

$n(\text{Co}^{3+})$, $n(\text{Co}^{\text{total}})$, and $n(\text{Co}^{2+})$ were the amount of Co^{3+}, total cobalt ions, and the amount of Co^{2+}, respectively. The total amount of cobalt ions was calculated on the basis of the ICP-OES results.

ICP-MS measurement for Cu and Al contents

ICP-MS was conducted using a Perkin Elmer Nexion 300 ICP-MS system. Cu [TraceCERT, Cu (1 g/liter) in nitric acid] and Al ICP standard solutions [TraceCERT, Al (1 g/liter) in nitric acid] were purchased from MilliporeSigma. The standard solutions were mixed and prepared at 1, 5, 10, 25, 50, and 1000 parts per billion. The sample concentration was calculated from the calibration curve.

GC-MS measurement for gas-phase products

Gases were captured in an evacuated flask and then injected onto a GC-MS (0.2 ml of injection volume) using a gas-tight syringe. The instrument is an Agilent 8890 GC equipped with an Agilent HP-5 ms low-bleed column (30 m, 0.25-mm internal diameter, 0.25-μm film) and using He carrier gas for liquid and headspace sampling. A tandem Agilent 5977B mass selective detector was used.

Economic and environmental analysis

The GREET 2020 and EverBatt 2020 software (58, 59), developed through Argonne National Laboratory, was used to estimate the cost and environment impact in adopting different recycling processes. For comparison, the cathode materials derived from virgin sources were also analyzed. Our analysis was focused on the cumulative energy use, GHG production, and the potential net profit during the various recycling processes. More detailed discussion can be seen in note S6.

Cathode resynthesis from the leachates

The gram-scale sample was prepared by VFD methods (shown in Table 2). FJH-activated BM samples (~1.5 g; including ~1.0 g of FJH-activated cathode waste and ~0.5 g of FJH-activated anode waste) were digested in 150 ml of 1.0 M HCl solution at 50°C for 90 min. The solution was filtered using a PES membrane (0.22 μm). The resulting solution was evaporated to a gel-like slurry and annealed at 450°C in air for 2 hours in the furnace. The obtained powder was ground with 20 wt % Li$_2$CO$_3$ for 15 min. The mixed powder was calcined at 800°C in air for 8 hours to produce the resynthesized LCO cathode material. A schematic diagram is shown in fig. S32.

Electrochemical performance test

To test the electrochemical performance of resynthesized LiCoO$_2$ cathode, the powder was mixed with PVDF and acetylene black at a mass ratio of 8:1:1 in NMP. The slurry was spread on carbon-coated Al foil (active mass loading of ~5 mg cm^{-2}) and dried in the oven overnight. The 2032-type coin cell was assembled by using Li metal foil as the anode and resynthesized LCO as the cathode inside an Ar-filled glovebox (O$_2$ content < 0.5 ppm, H$_2$O content < 0.5 ppm). Sixty microliters of 1.0 M LiPF$_6$ electrolyte (in EC:DMC:DEC = 1:1:1) and Al$_2$O$_3$-coated polypropylene were used

as the electrolyte and separator, respectively. The coin cells were charged and discharged on a battery working station (LANHE corporation, China) in air at 25°C. The test range of LCO cathode is 3.0 to 4.3 V versus Li^+/Li. After the initial three formation cycles at 0.1 cycling rate (C), the battery was tested at 0.2 C. The constant-current mode was used for the test.

Atomistic first-principles calculations

Partially graphitized carbon structures were obtained by simulated annealing of a large periodic cell containing 30,000 atoms with average density of 0.9 g cm^{-3}. Simulations were carried out with LAMMPS software package using AIREBO potential for interatomic interaction. After initial annealing at 400 K for 2×10^{-9} s, structures were heated to the target annealing temperature with a heating rate of 0.5×10^{-12} K s^{-1} using a Nose-Hoover thermostat (canonical NVT ensemble) with a temperature damping parameter of 0.025×10^{-12} s. The structures were held at the target annealing temperatures for 9×10^{-9} s.

Theoretical calculations of specific structural elements and phase energies were performed using first-principles density functional theory, as implemented in the VASP software package. Projector augmented wave (PAW) potentials are used for all species, and the wave functions were expanded in a plane wave basis with energy cutoff of 400 eV. All calculations are spin-polarized and use the Perdew-Burke-Ernzerhof exchange-correlation functional. Spin-orbit coupling was included in all the calculations. Rotationally invariant variant of the LSDA+U was used. All structures underwent unrestrained structural relaxation until the forces on all atoms were less than 10^{-3} eV $Å^{-1}$.

Supplementary Materials

This PDF file includes:
Supplementary Text
Notes S1 to S8
Figs. S1 to S43
Tables S1 to S7
References

REFERENCES AND NOTES

1. M. K. Tran, M.-T. F. Rodrigues, K. Kato, G. Babu, P. M. Ajayan, Deep eutectic solvents for cathode recycling of Li-ion batteries. *Nat. Energy* **4**, 339–345 (2019).
2. W. Lv, Z. Wang, H. Cao, Y. Sun, Y. Zhang, Z. Sun, A critical review and analysis on the recycling of spent lithium-ion batteries. *ACS Sustain. Chem. Eng.* **6**, 1504–1521 (2018).
3. M. S. Moats, W. G. Davenport, "Nickel and cobalt production," in *Treatise on Process Metallurgy: Industrial Processes* (Elsevier, 2014), vol. 3, pp. 625–669.
4. S. Natarajan, V. Aravindan, Recycling strategies for spent Li-ion battery mixed cathodes. *ACS Energy Lett.* **3**, 2101–2103 (2018).
5. M. Jacoby, It's time to get serious about recycling lithium-ion batteries. *Chem. Eng. News* 97, (2020). https://cen.acs.org/materials/energy-storage/time-serious-recycling-lithium/97/i28
6. Recycle spent batteries. *Nat. Energy* **4**, 253–253 (2019).
7. G. V. Rao, *Reference Module in Chemistry, Molecular Dciences and Chemical Engineering* (Elsevier, 2000), pp. 3491–3500.
8. A. Elshkaki, B. K. Reck, T. E. Graedel, Anthropogenic nickel supply, demand, and associated energy and water use. *Resour. Conserv. Recycl.* **125**, 300–307 (2017).
9. Q. Dehaine, L. T. Tijsseling, H. J. Glass, T. Törmänen, A. R. Butcher, Geometallurgy of cobalt ores: A review. *Miner. Eng.* **160**, 106656 (2021).
10. O. V. Martínez, J. Valio, A. S. Aarnio, M. Reuter, R. S. Guerrero, A critical review of lithium-ion battery recycling processes from a circular economy perspective. *Batteries* **5**, 68 (2019).
11. R. V. Salvatierra, W. Chen, J. M. Tour, What can be expected from "anode-free" lithium metal batteries? *Adv. Energy Sustain. Res.* **2**, 2000110 (2021).
12. X. Hu, E. Mousa, Y. Tian, G. Ye, Recovery of Co, Ni, Mn, and Li from Li-ion batteries by smelting reduction - Part I: A laboratory-scale study. *J. Power Sources* **483**, 228936 (2021).
13. Y. Tang, H. Xie, B. Zhang, X. Chen, Z. Zhao, J. Qu, P. Xing, H. Yin, Recovery and regeneration of LiCoO₂-based spent lithium-ion batteries by a carbothermic reduction vacuum pyrolysis approach: Controlling the recovery of CoO or Co. *Waste Manag.* **97**, 140–148 (2019).
14. M. Zhou, B. Li, J. Li, Z. Xu, Pyrometallurgical technology in the recycling of a spent lithium ion battery: Evolution and the challenge. *ACS EST Engg.* **1**, 1369–1382 (2021).
15. L. Li, E. Fan, Y. Guan, X. Zhang, Q. Xue, L. Wei, F. Wu, R. Chen, Sustainable recovery of cathode materials from spent lithium-ion batteries using lactic acid leaching system. *ACS Sustain. Chem. Eng.* **5**, 5224–5233 (2017).
16. L.-P. He, S.-Y. Sun, Y.-Y. Mu, X.-F. Song, J.-G. Yu, Recovery of lithium, nickel, cobalt, and manganese from spent lithium-ion batteries using l-tartaric acid as a leachant. *ACS Sustain. Chem. Eng.* **5**, 714–721 (2016).
17. A. Chagnes, B. Pospiech, A brief review on hydrometallurgical technologies for recycling spent lithium-ion batteries. *J. Chem. Technol. Biotechnol.* **88**, 1191–1199 (2013).
18. M. Sethurajan, S. Gaydardzhiev, Bioprocessing of spent lithium ion batteries for critical metals recovery – A review. *Resour. Conserv. Recycl.* **165**, 105225 (2021).
19. J. Xu, Y. Jin, K. Liu, N. Lyu, Z. Zhang, B. Sun, Q. Jin, H. Lu, H. Tian, X. Guo, D. Shanmukaraj, H. Wu, M. Li, M. Armand, G. Wang, A green and sustainable strategy toward lithium resources recycling from spent batteries. *Sci. Adv.* **8**, eabq7948 (2022).
20. N. Li, J. Guo, Z. Chang, H. Dang, X. Zhao, S. Ali, W. Li, H. Zhou, C. Sun, Aqueous leaching of lithium from simulated pyrometallurgical slag by sodium sulfate roasting. *RSC Adv.* **9**, 23908–23915 (2019).
21. Y. G. Yao, Z. N. Huang, P. F. Xie, S. D. Lacey, R. J. Jacob, H. Xie, F. J. Chen, A. M. Nie, T. C. Pu, M. Rehwoldt, D. W. Yu, M. R. Zachariah, C. Wang, R. Shahbazian-Yassar, J. Li, L. B. Hu, Carbothermal shock synthesis of high-entropy-alloy nanoparticles. *Science* **359**, 1489–1494 (2018).
22. C. Wang, W. Ping, Q. Bai, H. Cui, R. Hensleigh, R. Wang, A. H. Brozena, Z. Xu, J. Dai, Y. Pei, C. Zheng, G. Pastel, J. Gao, X. Wang, H. Wang, J.-C. Zhao, B. Yang, X. Zheng, J. Luo, Y. Mo, B. Dunn, L. Hu, A general method to synthesize and sinter bulk ceramics in seconds. *Science* **368**, 521–526 (2020).
23. D. X. Luong, K. V. Bets, W. A. Algozeeb, M. G. Stanford, C. Kittrell, W. Chen, R. V. Salvatierra, M. Q. Ren, E. A. McHugh, P. A. Advincula, Z. Wang, M. Bhatt, H. Guo, V. Mancevski, R. Shahsavari, B. I. Yakobson, J. M. Tour, Gram-scale bottom-up flash graphene synthesis. *Nature* **577**, 647–651 (2020).
24. B. Deng, Z. Wang, W. Chen, J. T. Li, D. X. Luong, R. A. Carter, G. Gao, B. I. Yakobson, Y. Zhao, J. M. Tour, Phase controlled synthesis of transition metal carbide nanocrystals by ultrafast flash Joule heating. *Nat. Commun.* **13**, 262 (2022).
25. W. Chen, Z. Wang, K. V. Bets, D. X. Luong, M. Ren, M. G. Stanford, E. A. McHugh, W. A. Algozeeb, H. Guo, G. Gao, B. Deng, J. Chen, J. T. Li, W. T. Carsten, B. I. Yakobson, J. M. Tour, Millisecond conversion of metastable 2D materials by flash Joule heating. *ACS Nano* **15**, 1282–1290 (2021).
26. W. Chen, C. Ge, J. T. Li, J. L. Beckham, Z. Yuan, K. M. Wyss, P. A. Advincula, L. Eddy, C. Kittrell, J. Chen, D. X. Luong, R. A. Carter, J. M. Tour, Heteroatom-doped flash graphene. *ACS Nano* **16**, 6646–6656 (2022).
27. Q. Dong, Y. Yao, S. Cheng, K. Alexopoulos, J. Gao, S. Srinivas, Y. Wang, Y. Pei, C. Zheng, A. H. Brozena, H. Zhao, X. Wang, H. E. Toraman, B. Yang, I. G. Kevrekidis, Y. Ju, D. G. Vlachos, D. Liu, L. Hu, Programmable heating and quenching for efficient thermochemical synthesis. *Nature* **605**, 470–476 (2022).
28. K. M. Wyss, R. D. D. Kleine, R. L. Couvreur, A. Kiziltas, D. F. Mielewski, J. M. Tour, Upcycling end-of-life vehicle waste plastic into flash graphene. *Comms. Eng.* **1**, 3 (2022).
29. P. Zhang, T. Yokoyama, O. Itabashi, T. M. Suzuki, K. Inoue, Hydrometallurgical process for recovery of metal values from spent lithium-ion secondary batteries. *Hydrometallurgy* **47**, 259–271 (1998).
30. Z. Zhu, D. Yu, Z. Shi, R. Gao, X. Xiao, I. Waluyo, M. Ge, Y. Dong, W. Xue, G. Xu, W.-K. Lee, A. Hunt, J. Li, Gradient-morph LiCoO₂ single crystals with stabilized energy density above 3400 Wh L^{-1}. *Energ. Environ. Sci.* **13**, 1865–1878 (2020).
31. B. Deng, X. Wang, D. X. Luong, R. A. Carter, Z. Wang, M. B. Tomson, J. M. Tour, Rare earth elements from waste. *Sci. Adv.* **8**, eabm3132 (2022).
32. W. Chen, R. V. Salvatierra, J. T. Li, D. X. Luong, J. L. Beckham, V. D. Li, N. La, J. Xu, J. M. Tour, Brushed metals for rechargeable metal batteries. *Adv. Mater.* **34**, e2202668 (2022).
33. B. Han, Y. Zou, G. Xu, S. Hu, Y. Kang, Y. Qian, J. Wu, X. Ma, J. Yao, T. Li, Z. Zhang, H. Meng, H. Wang, Y. Deng, J. Li, M. Gu, Additive stabilization of SEI on graphite observed using cryo-electron microscopy. *Energ. Environ. Sci.* **14**, 4882–4889 (2021).
34. Q. Zhang, J. Ma, L. Mei, J. Liu, Z. Li, J. Li, Z. Zeng, In situ TEM visualization of LiF nanosheet formation on the Cathode-Electrolyte Interphase (CEI) in liquid-electrolyte lithium-ion batteries. *Matter* **5**, 1235–1250 (2022).

35. M. Assefi, S. Maroufi, Y. Yamauchi, V. Sahajwalla, Pyrometallurgical recycling of Li-ion, Ni–Cd and Ni–MH batteries: A minireview. *Curr. Opin. Green Sustain. Chem.* **24**, 26–31 (2020).

36. J. Li, G. Wang, Z. Xu, Environmentally-friendly oxygen-free roasting/wet magnetic separation technology for in situ recycling cobalt, lithium carbonate and graphite from spent $LiCoO_2$/graphite lithium batteries. *J. Hazard. Mater.* **302**, 97–104 (2016).

37. W. A. Algozeeb, P. E. Savas, D. X. Luong, W. Chen, C. Kittrell, M. Bhat, R. Shahsavari, J. M. Tour, Flash graphene from plastic waste. *ACS Nano* **14**, 15595–15604 (2020).

38. W. Chen, J. T. Li, Z. Wang, W. A. Algozeeb, D. X. Luong, C. Kittrell, E. A. McHugh, P. A. Advincula, K. M. Wyss, J. L. Beckham, M. G. Stanford, B. Jiang, J. M. Tour, Ultrafast and controllable phase evolution by flash joule heating. *ACS Nano* **15**, 11158–11167 (2021).

39. B. Deng, P. A. Advincula, D. X. Luong, J. Zhou, B. Zhang, Z. Wang, E. A. McHugh, J. Chen, R. A. Carter, C. Kittrell, J. Lou, Y. Zhao, B. I. Yakobson, Y. Zhao, J. M. Tour, High-surface-area corundum nanoparticles by resistive hotspot-induced phase transformation. *Nat. Commun.* **13**, 5027 (2022).

40. X. Ma, M. Chen, Z. Zheng, D. Bullen, J. Wang, C. Harrison, E. Gratz, Y. Lin, Z. Yang, Y. Zhang, F. Wang, D. Robertson, S.-B. Son, I. Bloom, J. Wen, M. Ge, X. Xiao, W.-K. Lee, M. Tang, Q. Wang, J. Fu, Y. Zhang, B. C. Sousa, R. Arsenault, P. Karlson, N. Simon, Y. Wang, Recycled cathode materials enabled superior performance for lithium-ion batteries. *Joule* **5**, 2955–2970 (2021).

41. Y. Zheng, S. Wang, Y. Gao, T. Yang, Q. Zhou, W. Song, C. Zeng, H. Wu, C. Feng, J. Liu, Lithium nickel cobalt manganese oxide recovery via spray pyrolysis directly from the leachate of spent cathode scraps. *ACS Appl. Energy Mater.* **2**, 6952–6959 (2019).

42. S. P. Barik, G. Prabaharan, L. Kumar, Leaching and separation of Co and Mn from electrode materials of spent lithium-ion batteries using hydrochloric acid: Laboratory and pilot scale study. *J. Clean. Prod.* **147**, 37–43 (2017).

43. C. K. Lee, K. -I. Rhee, Reductive leaching of cathodic active materials from lithium ion battery wastes. *Hydrometallurgy* **68**, 5–10 (2003).

44. L. Li, R. Chen, F. Sun, F. Wu, J. Liu, Preparation of $LiCoO_2$ films from spent lithium-ion batteries by a combined recycling process. *Hydrometallurgy* **108**, 220–225 (2011).

45. S. -G. Zhu, W. -Z. He, G.-M. Li, X. Zhou, X. -J. Zhang, Recovery of Co and Li from spent lithium-ion batteries by combination method of acid leaching and chemical precipitation. *Trans. Nonferrous Met. Soc. China* **22**, 2274–2281 (2012).

46. L. Sun, K. Qiu, Vacuum pyrolysis and hydrometallurgical process for the recovery of valuable metals from spent lithium-ion batteries. *J. Hazard. Mater.* **194**, 378–384 (2011).

47. X. Zheng, W. Gao, X. Zhang, M. He, X. Lin, H. Cao, Y. Zhang, Z. Sun, Spent lithium-ion battery recycling – Reductive ammonia leaching of metals from cathode scrap by sodium sulphite. *Waste Manag.* **60**, 680–688 (2017).

48. Q. Li, K. Y. Fung, L. Xu, C. Wibowo, K. M. Ng, Process synthesis: Selective recovery of lithium from lithium-ion battery cathode materials. *Ind. Eng. Chem. Res.* **58**, 3118–3130 (2019).

49. H. Zou, E. Gratz, D. Apelian, Y. Wang, A novel method to recycle mixed cathode materials for lithium ion batteries. *Green Chem.* **15**, 1183–1191 (2013).

50. Y. Huang, G. Han, J. Liu, W. Chai, W. Wang, S. Yang, S. Su, A stepwise recovery of metals from hybrid cathodes of spent Li-ion batteries with leaching-flotation-precipitation process. *J. Power Sources* **325**, 555–564 (2016).

51. M. K. Jha, A. Kumari, A. K. Jha, V. Kumar, J. Hait, B. D. Pandey, Recovery of lithium and cobalt from waste lithium ion batteries of mobile phone. *Waste Manag.* **33**, 1890–1897 (2013).

52. M. Li, B. Zhang, X. Qu, M. Cai, D. Liu, F. Zhou, H. Xie, S. Gao, H. Yin, A $SiCl_4$-assisted roasting approach for recovering spent $LiCoO_2$ cathode. *ACS Sustainable Chem. Eng.* **10**, 8305–8313 (2022).

53. J. Xiao, J. Li, Z. Xu, Recycling metals from lithium ion battery by mechanical separation and vacuum metallurgy. *J. Hazard. Mater.* **338**, 124–131 (2017).

54. J. Xiao, J. Li, Z. Xu, Novel approach for in situ recovery of lithium carbonate from spent lithium ion batteries using vacuum metallurgy. *Environ. Sci. Technol.* **51**, 11960–11966 (2017).

55. J. Ndalamo, A. F. Mulaba-Bafubiandi, B. B. Mamba, UV/visible spectroscopic analysis of Co^{3+} and Co^{2+} during the dissolution of cobalt from mixed Co-Cu oxidized ores. *Int. J. Miner. Metall.* **18**, 260–269 (2011).

56. S. Sharifi-Asl, F. A. Soto, A. Nie, Y. Yuan, H. Asayesh-Ardakani, T. Foroozan, V. Yurkiv, B. Song, F. Mashayek, R. F. Klie, K. Amine, J. Lu, P. B. Balbuena, R. Shahbazian-Yassar, Facet-dependent thermal instability in $LiCoO_2$. *Nano Lett.* **17**, 2165–2171 (2017).

57. Y. Furushima, C. Yanagisawa, T. Nakagawa, Y. Aoki, N. Muraki, Thermal stability and kinetics of delithiated $LiCoO_2$. *J. Power Sources* **196**, 2260–2263 (2011).

58. Y. Liu, M. Wang, B. I. Yakobson, B. C. Wood, Assessing carbon-based anodes for lithium-ion batteries: A universal description of charge-transfer binding. *Phys. Rev. Lett.* **113**, 028304 (2014).

59. M. Wang, A. Elgowainy, U. Lee, A. Bafana, P. T. Benavides, A. Burnham, H. Cai, Q. Dai, U. R. Gracida-Alvarez, T. R. Hawkins, P. V. Jaquez, J. C. Kelly, H. Kwon, Z. Lu, X. Liu, L. Ou, P. Sun, O. Winjobi, H. Xu, E. Yoo, G. G. Zaimes, Summary of Expansions and Updates in GREET 2020 (2020 Report, Lemont, IL, USA).

60. Q. Dai, L. Gaines, J. Spangenberger, J. C. Kelly, S. Ahmed, M. Wang, Everbatt: A closed-loop battery recycling cost and environmental impacts model (2019); www.Anl.Gov/egs/everbatt.

61. J. Yu, J. Li, S. Zhang, F. Wei, Y. Liu, J. Li, Mechanochemical upcycling of spent $LiCoO_2$ to new $LiNi_{0.80}Co_{0.15}Al_{0.05}O_2$ battery: An atom economy strategy. *Proc. Natl. Acad. Sci. U.S.A.* **120**, e2217698120 (2023).

62. Z. Zhu, D. Yu, Y. Yang, C. Su, Y. Huang, Y. Dong, I. Waluyo, B. Wang, A. Hunt, X. Yao, J. Lee, W. Xue, J. Li, Gradient Li-rich oxide cathode particles immunized against oxygen release by a molten salt treatment. *Nat. Energy* **4**, 1049–1058 (2019).

63. J. Lee, C. Wang, R. Malik, Y. Dong, Y. Huang, D. -H. Seo, J. Li, Determining the criticality of Li-excess for disordered-rocksalt Li-ion battery cathodes. *Adv. Energy Mater.* **11**, 2100204 (2021).

64. W. Chen, "Joule heating routes for nanomaterial syntheses and surface modification for nanoscale applications," thesis, Rice University (2022). https://hdl.handle.net/1911/114222.

65. Scaleup of FJH for graphene synthesis; www.universalmatter.com/ [accessed 17 October 2022].

66. W. Chen, R. V. Salvatierra, J. T. Li, C. Kittrell, J. L. Beckham, K. M. Wyss, N. La, P. E. Savas, C. Ge, P. A. Advincula, P. Scotland, L. Eddy, B. Deng, Z. Yuan, J. M. Tour, Flash recycling of graphite anodes. *Adv. Mater.* **35**, 2207303 (2023).

67. T. Maiyalagan, K. A. Jarvis, S. Therese, P. J. Ferreira, A. Manthiram, Spinel-type lithium cobalt oxide as a bifunctional electrocatalyst for the oxygen evolution and oxygen reduction reactions. *Nat. Commun.* **5**, 3949 (2014).

68. W. Fan, Z. Ren, Z. Sun, X. Yao, B. Yildiz, J. Li, Synthesizing functional ceramic powders for solid oxide cells in minutes through thermal shock. *ACS Energy Lett.* **7**, 1223–1229 (2022).

69. W. Gu, P. Cheng, M. Tang, Compilation and evaluation of gas phase diffusion coefficients of halogenated organic compounds. *R. Soc. Open Sci.* **5**, 171936 (2018).

70. C. Zhang, K. Bets, S. S. Lee, Z. Sun, F. Mirri, V. L. Colvin, B. I. Yakobson, J. M. Tour, R. H. Hauge, Closed-edged graphene nanoribbons from large-diameter collapsed nanotubes. *ACS Nano* **6**, 6023–6032 (2012).

71. A. Miwa, T. Yajima, S. Itai, Prediction of suitable amount of water addition for wet granulation. *Int. J. Pharm.* **195**, 81–92 (2000).